Article submitted to: High Power Laser Science and Engineering, 2025 *July 24, 2025*

Thermal and hydrodynamical maquette study of water face-cooling for high average power laser amplifiers

Ch. Féral[1], D. Marion[1], J. Lhermite[1], D. Descamps[1], M. Lachat[1], M.-Ch. Nadeau[1], E. Mével[1], S. Petit[1], A. Rohm[1], D. Sarton[1], and Ph. Balcou[1]

[1]*Université de Bordeaux, CNRS, CEA, CELIA (Centre Lasers Intenses et Applications), UMR 5107, 33405 Talence, France*

Abstract

We report experimental optical and thermodynamical studies of convection cooling for face-cooling of laser amplifier disks. Amplifier maquettes are used to explore the flow regime in laser relevant conditions, and to measure heat exchange coefficients h. We thus benchmark analytical and numerical predictions, based on common models of turbulence. The y^+ model appears best suited to compute h in the laminar regime, and RANS in the weakly turbulent regime. By strioscopic imaging, we examine the optical properties of the flows, in particular the onset of a striation instability occurring well before the transition to turbulence. At higher Reynolds numbers, the unstable thermal layer is shown to be pushed back onto the surface, suppressing effectively the wavefront distortions from striations. This super-forced thermal regime may be of high interest for very high thermal loads.

Keywords: high average power lasers; face-cooling; striation instability; turbulence; heat exchanges

1. Introduction

High intensity and high energy laser research infrastructures are essential tools to explore physical processes of major potential importance, such as Inertial Fusion Energy[1], or Laser Wakefield Acceleration[2], with repetition rates for the current technological era of one to few shots per day for megajoule-class high energy lasers, and from 0.1 up to 10 Hz for ultra-intense titanium-sapphire laser systems. However, both of these flagship processes would require much higher repetition rates, and hence average powers, before they can be envisioned for actual energy supply, or lead to a new generation of compact particle accelerators.

Methods to increase the average powers of research-class intense lasers are therefore continuously investigated and improved. One key issue is thermal management: how can we efficiently remove the heat from laser crystals and laser amplifiers, without mitigating the optical qualities of the beam? An increasingly considered technological approach is the direct face cooling of laser slabs, either by helium at cryogenic temperatures[3,4], or by liquid coolants[5–8].

Both approaches have advantages and drawbacks: cryogenic helium cooling allows one to take advantage of a strongly enhanced emission cross section, at the price of the technological complexity of operating at cryogenic temperatures, and of a reduction of the amplification spectral width. Conversely, liquid face-cooling is easier to implement at room temperature, but has the disadvantage of being prone to complex thermo-hydrodynamic processes in the coolant, of which depends one crucial parameter, the h thermal exchange coefficient. Moreover, the onset of turbulences may degrade strongly the laser wavefront[9,10]. An empirical rule of fluid dynamics stipulates that the laminar/turbulent transition occurs when the Reynolds number increases beyond 2300[11,12]; however this value is simply indicative, and the hydrodynamics description of the phenomena at stake is highly complicated. Indeed, hydrodynamic instabilities may appear before the transition to weak turbulence, such as the streamwise oscillations called Tollmien-Schlichting waves, or turbulent spots. Finally, buoyancy forces inducing Rayleigh-Bénard-type instabilities may further complexify the processes at stake, particularly for natural or gently forced flows.

The complexity of these hydrodynamic issues is such that they gave rise to a huge number of scientific contributions, starting in the late 19th century. The laser physicist is therefore confronted with a hailstorm of analytical calculations, of empirical relations called correlations in hydrodynamics, and numerical approaches to model turbulence and instabilities, without the possibility to ascertain which formulae are relevant in a laser amplifier.

Correspondence to: Ph. Balcou, CELIA; Univ. Bordeaux, CNRS, CEA, 33400 Talence, France. Email: philippe.balcou@u-bordeaux.fr

10.1017/hpl.2025.10068

Laser-oriented studies of hydrodynamic and thermal issues of face-cooling in the specific conditions of split-disk laser amplifiers are therefore required.

Several numerical and theoretical works have started addressing this issue, in particular by solving numerically the Navier-Stokes (NS) equation on a grid, and focusing on some examples of flows chosen either in laminar, or on the contrary in fully developed turbulence conditions[9,13,14].

Li *et al.*[9] have chosen to investigate strongly turbulent flows, with a Reynolds number of 20000, with simulations based either on a 3D Reynolds time-averaged approach, hence a stationary approach, or on a time-dependent large-eddy simulation. In 2017, Nagymihaly *et al.*[15] have proposed to use water face-cooling to reach very high average power in titanium-sapphire thin-disks amplifiers, with numerical studies based on a Shear Stress Transport approach. A complementary numerical perspective was later brought by Yang[13], who discusses general coupled models to explain the entangled physics issues required to model the face-cooled crystal, from spectroscopic and thermo-optical properties of the laser medium, up to the fluid dynamics. While these contributions bring new insights into the highly complex physical phenomena occurring in the cooling of active laser media, it is not obvious to the laser scientist how to generalize these results to other sets of conditions.

A significant experimental effort is hence required, in parallel with the theoretical one, and several studies can be expected to be necessary before the full complexity of the issue is understood. In practice, a laser designer will generally seek to run numerical twins to the planned laser amplifier using sophisticated multi-physics software. That requires however to have a high level of confidence in simulation methods, implying that these were successfully benchmarked by experimental data beforehand.

The objective of our study is therefore twofold; i) characterize experimentally the flow regimes and heat exchanges in conditions directly relevant to laser slab amplifiers; and ii) benchmark and validate, or invalidate, the predictions of standard approaches from multi-physics modeling tools that describe jointly the hydrodynamics of the coolant flow, and the heat transport by conduction and convection, including turbulent transport.

Our experiments are based on specially designed maquettes, that fully reproduce the conditions of face-cooling of an amplifier slab, in terms of geometry, coolant flow characteristics, and heat loads; we also impose flow injection canals, identical to those used in current laser heads, meant to let the flow vorticity induced by the injection into the laser head decay before it gets in contact with the actual optical surface. Crucially, our maquettes are designed to allow for internal temperature measurements, enabling *in situ* determination of heat exchanges, and for optical diagnostics of the flow, based of the strioscopic method to characterize turbulence within the heated flow.

We then compare the results thus obtained with multi-physics modeling based on various approaches to describe turbulence within the Navier-Stokes equation, and on the diffusion-convection equation of heat transport. We also compare the data with some of the best known empirical or analytical formulae.

This article is organized as follows.

Section II first lists the essential concepts of hydrodynamics and energetics required for the study. Section III then presents the coolant flow characterization experiments, explains our experimental methods, and displays phase images from the two flow-transverse viewpoints, that show clearly the onset of flow instabilities. Section IV focuses on temperature measurements to diagnose the efficiency of heat extraction; these are compared with numerical and analytical predictions presented in section V. Section VI concludes on the main take-away messages from our studies, and proposes design strategies for the next generations of water face-cooled, very high average power laser amplifiers.

2. Relevant issues on hydrodynamics of forced flows between plane parallel plates, and heat exchanges

To facilitate reading by laser scientists, and for the sake of article consistency, we first remind some basics and key physical issues of hydrodynamics in the specific case of the flow used for face-cooling. We refer the reader to several excellent textbooks on the subject, especially[12,16–20].

2.1. *Hydrodynamics in Poiseuille flows*

A incompressible fluid flow inbetween two parallel and immobile walls follows a Poiseuille profile at low fluid velocities. The fluid velocity field is zero on the wall surfaces (no-slip condition), then follows a parabolic profile, with its maximum at the center between the plates. Streamlines remain straight and parallel; this flow regime is called laminar. The viscous forces are responsible for the regularity over the whole spacing between the walls; shear between layers advancing with different velocities is also minimal, resulting in a small value of pressure decrease along a forced laminar flow.

At higher velocities, the Poiseuille profile is disrupted, and the flow is no longer stationary neither in space nor in time. Flow vortices, also called eddies, appear randomly at large spatial scale, of the order of the spacing between walls, then break down into a cascade of smaller and smaller eddies. The downsizing continues until the eddies reach the Kolmogorov scale, which is the spatial scale at which viscosity imposes a locally regular, and hence vortex-less, flow. For standard coolants like water, and in our experimental conditions, the typical Kolmogorov length scale is of a few micrometers at most[16], as computed in section 5.2. This tiny value makes full simulations of flows in this regime, from the smallest to the largest eddies, very difficult. This regime

https://doi.org/10.1017/hpl.2025.10068 Published online by Cambridge University Press

is called turbulent, with a first range of velocities with weak turbulence, also called transitional regime, then fully developed turbulence at very high velocities.

One key parameter, the Reynolds number *Re*, allows to describe the transition between laminar and weakly turbulent or transitional, and from weakly turbulent to fully turbulent:

$$Re = \frac{d \cdot v_0}{\nu}, \tag{1}$$

where v_0 is the incoming flow velocity, equivalently given as the velocity average in the duct; d is a characteristic transverse scale length of the duct; and ν is the kinematic viscosity, equal to the dynamic viscosity divided by the coolant specific mass. The Reynolds number can be considered as the ratio between the inertial forces ($\propto dv_0$) and viscosity forces ($\propto \nu$)[19]. The Reynolds number can be defined in several context-dependent ways, resulting from the definition of the characteristic length d. In the present study, we use throughout the definition of the Reynolds number commonly used in engineering, where $d = d_h$ is the hydraulic diameter, defined as four times the ratio between the duct area and its wet perimeter[20]. With this definition, the length is reduced to the ordinary diameter in the case of a circular duct. For a rectangular duct of high aspect ratio, especially the water canals used in face-cooling, it is close to the twice the canal width. Some authors have advocated other definitions for rectangular ducts or canals[18]. We found however the usual engineering definition accurate to describe our experimental findings.

Transition between laminar and weakly turbulent is usually considered to happen around $Re = 2300$[11,12], although this may strongly vary, eg if the incoming flow has a non zero intrinsic vorticity, if the wall surfaces are irregular, in the presence of strong sound waves, etc. However, the transition to turbulence is the result of more complex processes occurring at lower Reynolds numbers, also called pre-transitional processes, the most important, but not the sole one, being the Tollmien-Schlichting (TS) instability. TS waves are oscillatory features of the physical parameters along the flow; the oscillatory part of the velocity follows a vortex-like pattern with alternate helicities transverse to the flow – akin to ocean wave rolls. The flow is therefore purely one-dimensional at low Reynolds numbers, becomes two-dimensional at the onset of the TS instability, and eventually three-dimensional when the TS rolls break into secondary waves, triggering the onset of weak turbulence.

The physics of instabilities and of the laminar-to-turbulent transition in boundary layers is fully described in[18].

2.2. *Heat exchange in Poiseuille flow*

The physics of heat exchanges between the walls and a fluid in a Poiseuille flow was first addressed by Graetz as early as 1885[21], so that the issue of heat exchange in a Poiseuille flow is known as the Graetz, or Graetz-Nusselt problem.

Figure 1: Example of thermal layer within a Poiseuille flow, as computed numerically in section 5.2, in the experimental conditions of Figure 12(a), and a flow velocity of 0.3 m/s. The flow direction is from left to right. The color indicates the copper and water temperature distribution, in Celsius. Thin black lines delineate the copper and water frontiers.

The textbook by Battaglia, Kosiak and Puiggali supplies the modern reference formulae and their domains of validity[22].

In a flow past a single wall (Blasius flow) with heat exchanges, one distinguishes a thermal boundary layer from the momentum or velocity boundary layer. The ratio between the widths of the latter to the former is given by material-dependent dimensionless number, the Prandtl number *Pr*. In water, $Pr = 7$, so the thermal layer is consistently smaller than the momentum layer.

In a fully developed and stationary Poiseuille flow, the velocity transverse distribution follows a quadratic law, so that the notion of momentum boundary layer disappears, and the thermally affected zone may either consist of a thin layer next to the exchange wall, or occupy the whole flow, when the heat exchange takes place over a long length. Figure 1 shows a typical thermal layer in the former condition, as computed in section 5.3 based on our experimental conditions. By continuity, the temperature of water in touch with the wall is equal to the wall temperature; at the canal center, it is equal to the incident flow temperature T_0. These extrema are separated by a thin thermal layer, whose width increases from few tens of micrometers at the entrance, to about 200 μm at the exit in these conditions. We will assume in the following that we stick to the conditions where the thermally affected zone is a thin layer, which are the optimal conditions to cool a laser slab.

The heat exchange itself is described by an exchange coefficient h, in $Wm^{-2}K^{-1}$, or by a dimensionless number, the Nusselt number :

$$Nu = \frac{h.d}{\lambda}, \tag{2}$$

where λ is the heat conductivity of the fluid, and d the characteristic length scale introduced above. As the temperature distribution along the flow depends on the streamwise position, the Nusselt number is defined locally; a overall Nusselt number can be obtained by averaging over all local Nusselt numbers.

https://doi.org/10.1017/hpl.2025.10068 Published online by Cambridge University Press

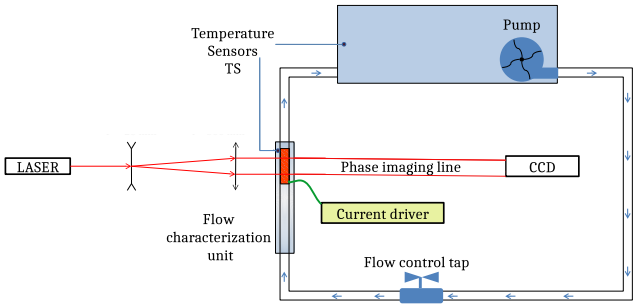

Figure 2: General experimental setup for optical characterizations of flow inhomogeneities as a function of flow velocity and resulting Reynolds number.

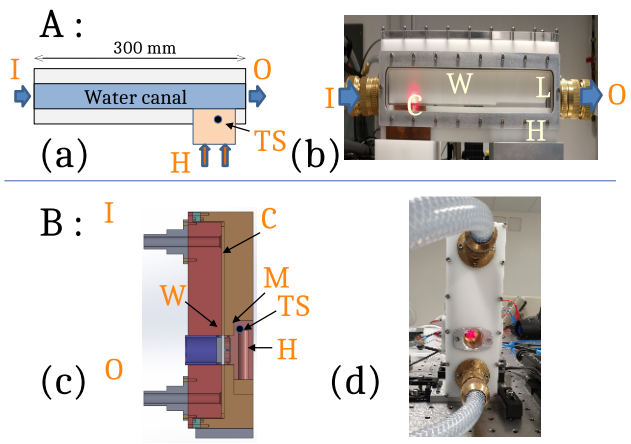

Figure 3: Scheme and pictures of the visualization maquettes of forced flows under strong heat load. (a) and (b): maquette A, in-flow transverse imaging setup; (c) and (d): maquette B, laser-axis imaging. Component labels; I: inlet; O: outlet; C: water canal; H: electrical heater; W: optical window; M: copper mirror; L: probe laser; TS: temperature sensor.

3. Flow visualization studies: from laminar to striation instability and onset of weak turbulence

Few investigations of laser wavefront quality after propagation through real face-cooled laser amplifiers have already been presented. Some of these studies report pictures of unexpected phase perturbations of the spatial profile, in the shape of streaks, also called striae, mostly oriented along the coolant flow[10,23]. To the best of our knowledge, no systematic study has been reported; this behavior is sometimes considered as a manifestation of weak turbulence.

To investigate both qualitatively and quantitatively the loss in wavefront quality, we have designed a general beam qualification setup, with two complementary maquettes of a face-cooled amplifier head, in which optical observation of flow temperature inhomogeneities in the flow is made possible by strioscopy, along two observation axes: transverse (sidewise), and axial (along laser axis).

3.1. Experimental setup

Figure 2 first displays the general experimental setup, as a top view of the optical table. Three major components can be distinguished: the flow characterization head, the hydraulic circuit with controls and sensors, and the optical imaging line.

The hydraulic circuit is meant to inject a controllable flow of deionized water into the flow unit, by means of a pump delivering a digitally controlled over-pressure, and of a manual flow control tap. Water exiting the unit enters a large reservoir where it is thermalized to room temperature. Water temperature is monitored by a sensor located within the tank, with a precision of 0.1 °C. Water is derived from the tap, and used after a deionization and filtering step. No pH control appeared necessary for these experiments.

A rigorous measurement of the volumetric flow rate F is essential for the determination of the fluid velocity within the maquette, and hence of the Reynolds number. Two methods were used: 1) an ultrasonic flow-meter for high flows, from $2\,l/min$ onward, and 2) chronometry of water filling a calibrated beaker for low flows, namely from zero up to typically $4\,l/min$, with a relative accuracy related to the timing precision – hence a somehow cumbersome method, but accurate in absolute value. The intermediate flow region for which both methods are possible was used to calibrate the ultrasonic flow-meter, so that absolute flow values could be inferred over the whole range of flows. The average flow velocity within the maquette canal of cross-sectional area S is then simply given by $v_0 = F/S$. The canal transverse sizes were 30 and 40 mm uniformly for maquettes A and B respectively, so that the hydraulic diameters are almost equal to twice the canal widths.

3.2. Amplifier maquettes for flow visualization

Figure 3 presents the two amplifier maquettes used for the hydrodynamic studies of flows in a heated amplifier-like environment. They are designed to image transversely the thermal effects arising along the flows, in laminar and turbulent regimes. Imaging is performed either sideways in the plane of the flow (maquette A), or along the laser axis, orthogonal to the plane of the flow (maquette B). The liquid-cooled laser amplifying medium is replaced by a copper block, or heel, in which two elements are embedded: a heating thermistor (H), in which up to 100 W heat can be generated, and a small (4 mm diameter) temperature sensor (TS). The heel has a flat and highly polished surface, brought in contact with a steady water flow; the temperature sensor in located close to the surface (2 mm), and at the geometrical center of the exchange surface.

Maquette A (cf Figure 3(a) and (b)) thus features an horizontal water canal, 300 mm long, in which the last section before the water outlet corresponds to a 60 mm

https://doi.org/10.1017/hpl.2025.10068 Published online by Cambridge University Press

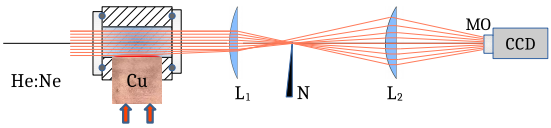

Figure 4: Principle of the strioscopic technique used to visualize flow index inhomogeneities within the flow characterization unit. Component labels; He:Ne: Helium-Neon laser; Cu: copper heel; L_1 and L_2: lenses; N: needle; MO: microscope objective; CCD: charged coupled device camera.

heated copper surface. The canal width can be varied from 0.5 mm up to 3 mm; the 240 mm long entrance section is intended to let the turbulence induced by the water injection decay, so that the flow has reach its fully developed profile upon arriving on the heat flux section.

In contrast, the flow plane is vertical in maquette B (cf Figure 3(c) and (d)), with a introduction turbulence decay section of 120 mm, that leads the flow onto a 1-inch circular mirror, made of copper with a gold layer. This configuration was chosen to allow for optical-quality reflection of the probe laser onto the mirror, while keeping an optimal thermal coupling. The probe laser therefore makes a round-trip within the coolant flow, thus doubling the phase disturbances. Indeed, any flow inhomogeneity or turbulence in the incident cold fluid, once in contact with the hot surface, results in the appearance of fluid elements with spatially varying temperatures, leading to inhomogeneous optical indices. We characterise these by a standard strioscopic method, depicted in Figure 4. A helium-neon probe laser, of high spatial quality, goes through the water canals of the various maquettes, then is focused, yielding an intermediate far-field plane, in which a mask removes the central spatial frequencies. The standard circular mask of the strioscopic method is replaced here by a needle. Only the higher spatial frequencies, induced by the phase object, in our case the water canal, are transmitted. The exit plane of the water canal is then imaged onto a CCD camera; this yields an image of the phase retardances of the water phase object[24,25].

3.3. In-plane transverse imaging

Maquette A, and the strioscopic imaging setup of Fig. 4 were used to explore qualitatively how the flow, and the boundary layers evolve as the flow speed increases from 0. The onset of the laminar regime, followed by the first signs of flow inhomogeneities, are best seen dynamically on a video, available on Zenodo at[26]. In this video, the coolant is set in motion by gradual opening of the flow control tap, from a closed position at time 0, up to full opening. The indicator on top left yields the temperature value, in $°C$, from the temperature sensor.

From this video, Figure 5 and Figure 6 present snapshots,

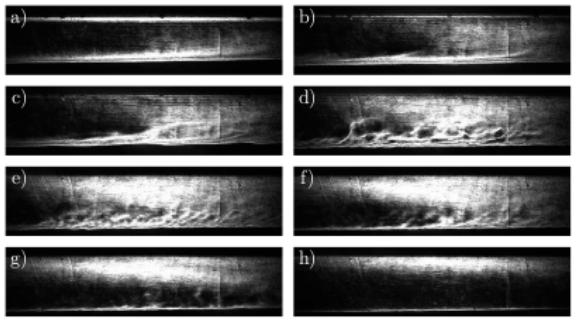

Figure 5: Series of transverse strioscopic images of the flow when the water flux is gradually increased from laminar to turbulent, and eventually super-forced thermal regimes. Canal width : 3 mm. Water flows from left to right. Heating occurs on the lower surface. Re=2100 in fig. (b), Re=14000 in fig. (h).

with increasing flow velocities. In Figure 5, the field of view encompasses all of the 3-mm width of the canal; a thermal boundary layer appears clearly on top of the lower wall, on all images. The upper wall of the canal should not give rise to strong thermal exchanges; it appears nevertheless on the first images.

(a) corresponds to a slow flow, in the laminar regime; one observes clearly an expanding thermal layer, with a thickness growing linearly along the flow. In (b), "plumes" start to appear above the thermal layer, without affecting the previously mentioned linear behavior; irregularities appear in (c). The Reynolds number in (b) was 2100, as measured in a following experiment stopped at this flow level. Increasing the flow further, the thermal layer becomes turbulent in (d), with obvious signs of random eddies in the middle of the flow. Upon increasing the flow further in (e), the vortices start earlier, and tend to to decrease in size. The behaviour of the thermal layer is especially striking in images (f), (g) and (h), as the eddies appear to be pushed back onto the lower surface, and decrease in size and in luminosity. In the final image, (h), obtained at the highest flow velocity (Re=14000), the thermal layer is squeezed back onto the lower surface, with no irregularity in light diffusion, and is restricted to a thin regular line.

Numerous works in hydrodynamics explain that, once a turbulent regime is set, there is no possibility that the turbulence, and the random eddies, may vanish upon increasing the flow velocity. What we observe in this optical method are the inhomogeneities of the optical index, resulting from spatial variations in temperatures; therefore, we can conclude that, at high velocities, hence well into the weakly turbulent regime, the heat extraction is so efficient that the temperature is actually quasi-homogeneous in the whole canal, except in the immediate vicinity of the heating surface.

The wavefront dephasings on the upper half of the canal, next to the non-heated wall, features an interesting behaviour. On figure (a), a second upper thermal layer is clear,

https://doi.org/10.1017/hpl.2025.10068 Published online by Cambridge University Press

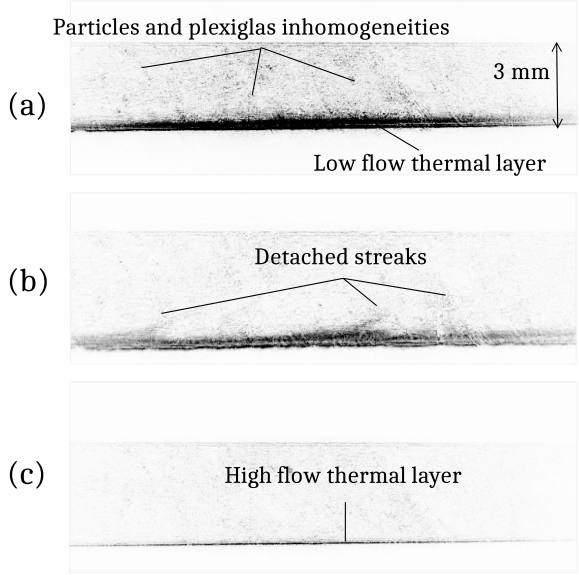

Figure 6: Zoom on the heated layer (inverted strioscopic imaging mode) in (a) laminar regime; (b) instable streaks detached from the wall (Re= 2100); (c) super-forced thermal regime, with the thermal layer squeezed onto the exchange wall.

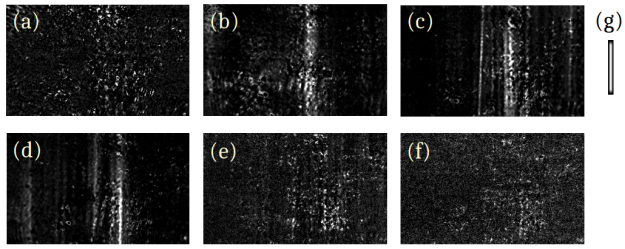

Figure 7: Near-field views displaying the streamwise streaks for different flow rates, and hence different Reynolds numbers: (a); Re=1100; (b), Re=2000; (c) and (d), Re=2300; (e), Re=5000; (f), Re= 10800. (g): model stria used to extract the striation level from each image, from a shape recognition method.

which appears along the flow at the same position as the main lower thermal layer; in contrast to the lower layer, its width remains constant, and consistent with the upper viscous sub-layer. This linear and thin upper thermal layer is still visible on figure (b), but vanishes at higher flows, and is replaced by a broad and homogeneous distribution of thermal dephasings, with its maximum in width and brightness in (e) and (f). The evolution in the upper canal part may be interpreted as resulting from hot fluid elements leaving the main thermal layer where this layer is largest, which then slow down in the upper slow layers of the Poiseuille flow; and possibly setting a thermal equilibrium with the low-effusivity glass that constitutes the upper canal wall. In a real multi-slab amplifier, a similar configuration might arise in the lateral water canals, in-between the first and last slabs, and their glass window counterparts.

Figure 6 displays three zooms over the thermal layer, for increasing flow velocities. For visual clarity, we have inverted the black-and-white color code, thus showing the heated flow regions in black, and the cold regions in white. Figure 6(a) corresponds to a laminar regime; the mesh of tiny black spots in the middle of the flow can be assumed to correspond to phase defects in the imaging line itself, possibly in the plexiglass windows, or to defects in the water flow.

Figure 6(b) is taken shortly after the appearance of the first inhomogeneities in the flow; threads of heated water can be seen, leaving the thermal layer, and directed to the center of the flow. Finally Figure 6(c) is a zoom of one of the last images of[26], obtained at high flow. This picture shows in a spectacular way how the high flow compresses the thermal layer onto the surface, and displays no sign of the internal flow vortices, known to exist at high velocities. In this super-forced thermal regime, the very high convection effectively bleaches out the effects of thermal inhomogeneities.

3.4. Axial imaging: onset of striation instability

Strioscopic imaging, still transverse to the flow but along the laser axis, allows one to image directly the wavefront perturbations that are imposed on a laser by the flow inhomogeneities. Our results are close to those obtained by Dalbies *et al.*[23] with a Foucault-knife approach.

We have used the axial strioscopic setup to shoot movies of the time evolution of the transmitted wavefront. From those movies, we have selected some of the most distinctive images. Figure (7) thus displays the phase perturbations for five different flow velocities, characterized by their Reynolds numbers Re of 1100 (a), 2000 (b), 2300 (c and d), 5000 (e), and 10800 (f). The size of the rectangular region of interest displayed is 6.38 mm $\times$ 3.85 mm.

Images in Figure 7(b), (c) and (d) exhibit clear wavefront striae, as reported by Ruan *et al.*[10] and Dalbies *et al.*[23]. These striae appear randomly on a black background, meaning that most of the wavefront is undisturbed; striae on these strioscopic phase images indicate that current threads with higher temperature than the surrounding fluid appear in an apparent random way. Such hot current threads can be seen to be essentially parallel to the general direction flow; slight deviation angles with respect to the vertical direction may be seen occasionally, which remain compatible with possible local and transient deviations of the flow.

Images in Figure 7(a), (e) and (f) show much fainter striae, not necessarily on all images. We have not seen any stria on flows with a Reynolds numbers less than 1000. On the high velocity side, hazy striae can still be perceived at Re=10800 on few images. Our setup did not allow us to reach even higher Reynolds numbers.

From each of the numerous images constituting the wave-

https://doi.org/10.1017/hpl.2025.10068 Published online by Cambridge University Press

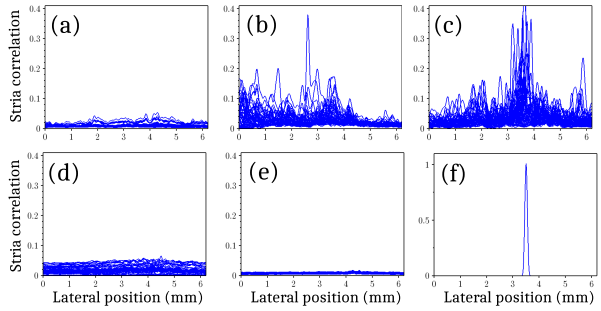

Figure 8: Superposition of correlation functions of all images with the model stria for different flow rates: (a); *Re*=1100; (b), *Re*=2000; (c), *Re*=2300; (d), *Re*=5000; (e), *Re*= 10800. (f): correlation function between an ideal stria, and the stria template.

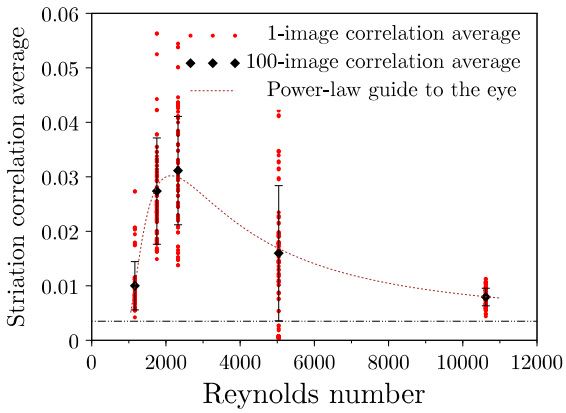

Figure 9: Reynolds number dependence of the average striae correlation. Dashed bottom line : residual correlation with the random background of the images, which defines the lower limit of significant correlations.

front movies taken for each Reynolds number, it is necessary to infer a quantitative estimate of the incidence of striae in the region of interest. This required to develop a numerical method, mostly based on the well-known OpenCV library of image analysis.

As the striae can be of small amplitude, hardly visible among the noise, it is first necessary to subtract carefully the static background image. The latter is identified by a statistical analysis of the distribution of counts on each pixel of the region of interest, after an homothetical reduction by a factor 3. Each background-free image then is subjected to a shape-recognition algorithm, in which the template shape is the model stria displayed in Figure 7(g). We use the normalized shape correlation method, which, for each image, outputs a matrix of correlations with the template stria. As the latter is vertical, we take the maximum correlation value for each column; this yields an horizontal correlation function, displayed in blue in Figure 8. Sub-panel (f) illustrates the case of a mathematically defined perfect stria, extending vertically at an arbitrary horizontal position. The algorithm correctly presents a correlation peak up to 1 at the central position of the ideal stria, and yields null values on black zones.

In Figure 8(a) to (e), the striae correlation functions obtained for 100 successive images of the captured movie are superposed, for the same Reynolds number as for Figure 7. Each high peak in these correlations functions denotes the existence of one strong stria; different behaviors can be immediately noticed. In Figure 8(c), a strong concentration close to the center of the image is clear; in figure (b), the same zone also features regularly striae, but the left-hand side part of the image also presents many correlations peaks. The distribution of striae is much more uniform in Figure 8(d). These differing preferential zones of stria appearance may be related to slightly different flow conditions, or remaining vorticities, for the various velocities. Apart from the preferential zones, one also notices that there is no fixed or repeated position; hence the stria are not formed on a specific defect sites upstream, but appear randomly. We should mention however that, in early designs, we did observe occasionally striae arising at a fixed position, suggesting they can also stem from surface defects; only after a careful mechanical design to remove any such defect did we observe the randomness in striae positions.

Figure 9 displays the average values of the striae correlation function for each of the 100 images (red points), and the overall average of the average values (black diamond), as a function of the Reynolds numbers of the five flows studied. The background images yield a low but non-zero average of the spatial correlation function; hence the bottom line indicated in dashes. No striae are seen below $Re = 1000$; then the average striae correlation grows suddenly up to a maximum around 2500. The measured striae then start decreasing down to almost zero for $Re \simeq 10000$. The dotted line is a simple guide to the eye, taken as the the product of two power law dependencies, one increasing sharply from $Re = 1000$ on, and one decreasing steadily from zero.

3.5. Discussion on the optical striation instability, and hydrodynamic streaks

The appearance of striae in face-cooling was not anticipated, and their physical origin remains uncertain. Some authors mention them as an effect of turbulence; we suggest that these striae are the result of a hydrodynamic instability, in the same range of Reynolds numbers as the Tollmien-Schlichting instability, but are well distinct from weak turbulence. Indeed, in an axial view, the striae appear as extremely straight and regular over lengths possibly exceeding several centimeters – as demonstrated in Dalbies et al.[23]. No meandering was observed, although the striae may appear as non fully parallel to the main flow, in rare cases. This

https://doi.org/10.1017/hpl.2025.10068 Published online by Cambridge University Press

seems however incompatible with the random interplay of flow vortices inherent to a turbulent regime.

Secondly, the striae do not systematically appear; some pictures were essentially free of any striation; and other pictures show striae in some areas, and no wavefront perturbations in others. Again, this is not a behaviour of a turbulent flow.

Thirdly, we observe a sudden rise in the prevalence of striations from $Re = 1000$ onward, whereas the results of the following section on heat exchanges demonstrates the onset of the weakly turbulent regime at $Re \simeq 2700$, consistent with the standard values reported in the scientific literature [11,12,20].

We conclude that the striae are the result of a pre-transitional hydrodynamic instability, and not of weak turbulence. This leaves open the issue of the physical origin of this instability.

We propose at this stage a naming convention: in the optical community, the long lines observed are most often called "striae", consistent with the fact that they are actually phase retardances observed by strioscopy or any equivalent technique. In the hydrodynamics community, long linear structures are usually called streaks, and thought of as a line of current with different velocities, pressure, and shear concentration as the surrounding flow. We suggest to keep both wordings, "striae" whenever we refer to the optical structures, and "streaks" when we refer to the underlying hydrodynamical structure.

To the best of our knowledge, the streaks within the boundary layer of a Poiseuille flow at an early stage of the laminar-to-turbulent transition did not attract much interest in the field of hydrodynamics and of heat exchanges. Situation is however different for Blasius flows, with a number of works studying the physics of longitudinal flow streaks and their role in the chain of processes that eventually trigger turbulence (see Boiko [18], chapter 9, and references therein).

As concerns specifically Poiseuille flows, as an introduction to his work on the induction of instabilities in the plane Poiseuille flow, Mizushima [27] does not mention any case of streak formation; on the contrary, his first-principle calculations result in the well-known Tollmien-Schlichting (TS) instability, ie, rows of vortices of alternate helicities, with axes transverse to the flow, as illustrated by Barahona *et al* [28] (Figure 9). Many other contributions explore the physics of the Tollmien-Schlichting instability. From this body of work, we can conclude that TS waves and face-cooling striae display entirely different geometries, and are therefore two distinct processes.

From the scientific literature on hydrodynamics of unstable plane flows, we found however two processes displaying current streaks in Poiseuille flows.

Several studies have indeed been devoted to the "low speed streaks" appearing in transitional planar flows, at higher Reynolds numbers; these streaks were first observed by Kline *et al* [29] (Figure 10), and were subject later to extensive research works reviewed by Lee and Wu [30]. In addition to the higher Reynolds regime, the characteristics of those low speed streaks are wholly different: they present a high level of self-organization, with an initial regular pattern, similar intensities, and quickly display meandering and mixing behaviours. None of these features are observed on the striae seen in face-cooling.

In the laminar regime of natural convection between a heated vertical wall and a passive wall, Colak-Antić and Görtler reported on vertical striae whose visual appearance is extremely similar to those of face-cooling. The striae were first observed in a low Reynolds laminar regime (figure 3(a) of [31]), then in conjunction with Tollmien-Schlichting waves at larger Reynolds numbers – confirming these are two different processes, starting at different Reynolds numbers in natural convection.

The existence and role of streamwise streaks in Blasius flows, of direct interest in aerodynamics, received much more attention. In their textbook [32], Boiko *et al.* survey several instabilities observed in pre-transitional flows, in addition to Tollmien-Schlichting waves: Λ-shaped structures, turbulent spots, and puffs resulting from a well-studied lift-up mechanism, and may extend over many characteristic lengths d in the streamwise direction. This feature makes puffs interesting candidates to explain the striae observed in liquid face-cooling, provided the physics in Blasius flows can be extended to Poiseuille flows. However, the striae could also result from a process that couples thermal and hydrodynamic processes, through the temperature dependence of density and viscosity.

More detailed hydrodynamical studies would hence be required to ascertain the intrinsic nature of the striation instability. In the scope of the present study, were merely point out that some instabilities, like the puff instability, coupled to a hot wall, might result in the appearance of streaks, with a differential heating from the main flow resulting in locally different temperatures, inducing wavefront distortions by virtue of the temperature dependence of the refractive index.

4. Experimental study of heat exchange coefficient in laser- amplifier-relevant conditions

We now turn to the study of the heat exchange coefficients, or Nusselt numbers, based on a third maquette design, allowing one to control the amount of heat deposited in the coolant, and to measure precisely inner temperature, and input and output water temperatures.

4.1. Measurement method for the heat exchange coefficient

Maquette C, schematized in Figure 10(a) and pictured in Figure 10(b), is designed to perform the measurement of the exchange coefficient, in flow and thermal load conditions similar to those of a multi-slab laser amplifier.

https://doi.org/10.1017/hpl.2025.10068 Published online by Cambridge University Press

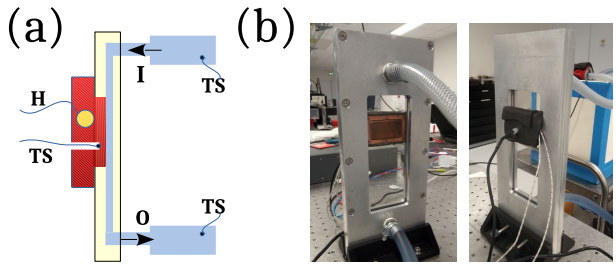

Figure 10: Scheme (a) and pictures (b) of the exchange coefficient measurement maquette. Component labels; I: inlet; O: outlet; H: electrical heater; TS: temperature sensors.

The thermal heel is a 20 mm-thick copper block, whose exchange surface with the liquid coolant is a rectangle of 24 mm (along the flow) by 50 mm (transverse to the flow). As the overall, and measured, exchange coefficient depends on the length of the exchange zone along the flow, this rectangular geometry allows us to infer an unambiguous h coefficient.

Figure 11(a) shows a semi-transparent view of the copper block (yellow), positioned in an optically transparent but thermally isolating PMMA optical window (grey). The exchange surface ES is grazing to the inner surface of the optical window, in order to prevent any induced vorticity in the water flow. The temperature sensor TS is embedded deeply within the copper block, just 2 mm from the exchange surface. In a coordinate frame where x and y are respectively transverse and along the flow, with an origin at the center of the exchange rectangle, the temperature sensor stands at $x = 0$ and $y = +5$ mm. The heater is a cylinder-shaped resistor, also embedded within the copper block These mechanical details happen to have an importance to compute the apparatus response function.

Indeed, the heat exchange coefficient h is defined as[20] :

$$h = \frac{P_{th}}{S(T_{av} - T_0)}, \tag{3}$$

where P_{th} is the thermal power load, S the exchange surface, and T_{av} the average temperature on the exchange surface; whereas the experiment yields an exchange coefficient as :

$$h_{\text{measured}} = \frac{P_{th}}{S \cdot (T_{TS} - T_0)}.$$

where T_{TS} is the temperature as measured by the embedded temperature sensor, which is not strictly equal to the average temperature on the exchange surface. This systematic error is expected to be small, since we chose copper as constituent material, whose high thermal conductivity should lead to an optimally homogeneous temperature over the block. However, the heat flow is never homogeneous – neither for our device, that includes a localized heater and an insertion hole for the temperature sensor; nor for a real laser amplifier slab, for which the heat flow depends on the volumetric heat generation. Moreover, the heat flux can also be partly evacuated by other channels than conduction through the exchange surface with the coolant. Such corrections are again expected to be minor, but should be evaluated. All these processes are related to thermal conduction and exchanges in the copper block, which are well known, and can be modeled numerically with high accuracy.

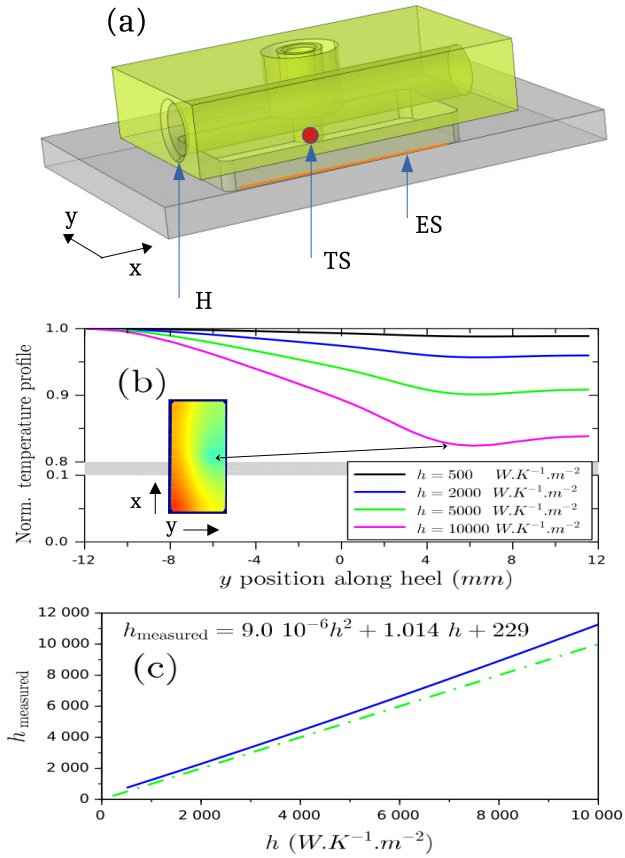

Figure 11: Numerical calibration of the exchange coefficient h: (a), geometry of the 3D numerical twin. H: heater; TS : temperature sensor; ES: exchange surface. (b) normalized temperature profiles predicted for different target values of h; Inset : temperature profile over the exchange surface, from cyan (coldest) to red (hottest), for h=10 000 $W.K^{-1}.m^{-2}$. (c) exchange coefficient predicted to be measured, versus input exchange coefficient.

To determine the response function, we therefore use a numerical twin of the setup, by means of a COMSOL® simulation. Starting from a given exchange coefficient h, and for an arbitrary heater power, we compute the temperature profile in the block, then at the temperature T_{TS} at the position of the sensor, leading to a numerical evaluation of h_{measured}.

Figure 11(b) shows the normalized temperature profile $(T-T_0)/(T_{\max}-T_0)$ on a line of the exchange surface, in the

https://doi.org/10.1017/hpl.2025.10068 Published online by Cambridge University Press

y direction parallel to the flow, and going through the sensor ($x = 0$), for different exchange coefficients, from a low value (500 W/K/m^2) up to a high value (10000 W/K/m^2). We took a constant copper-to-air exchange coefficient of 50 W/K/m^2. At low exchange coefficients, the profile can be seen to be regular and close to 1, implying that the sensor provides a satisfactory estimate for the mean temperature; in contrast, high exchange coefficients lead to somehow lower temperatures and more pronounced inhomogeneities. The inset shows a false-color map of the temperature over the exchange surface, from cyan to red, for the highest exchange coefficient. A temperature minimum, and a kink in the profile, appear right below the position of the temperature sensor, leading to a noticeable deviation between the temperature at the sensor position and the average temperature.

Figure 11(c) displays the numerical prediction of the measured exchange coefficient as a function of the exchange coefficient taken as input. To help the eye, the dot-dashed line shows for comparison the identity curve : $h_{\text{measured}} = h$. The response function appears fairly linear, with however a small quadratic term, that leads to a deviation up to 10 % for the highest values of h. A small constant term results from the cooling action of air convection at the copper to air interfaces, negligible for high values of h.

This response function can now be inverted to correct the experimental exchange coefficients presented in the next section.

4.2. Experimental results on heat exchange coefficients

Figure 12 shows the experimental data on heat exchange coefficients obtained with maquette C, with a water canal of 0.54 mm width (a), and 1.1 mm width (b). In the latter case, two independent measurement series were performed several days apart, and are labelled measurement set 1 (circles) and set 2 (dots).

We supply error bars along both abscissa and ordinates. The uncertainties on the flow velocities result i) from the uncertainty on the flow measurement with the chronometry method, estimated to $\pm 5\%$ (timing uncertainty about 1 s over 20 s , meniscus height of the water surface of 1 mm in a 150-mm beaker); and ii) from the uncertainty on the width of the canal, estimated to $\pm 25 \mu m$ in absolute value. Combining these uncertainties results in velocity error bars of $\pm 7\%$ and $\pm 6\%$ for the 0.54 mm and 1.1 mm canals respectively. The uncertainties on h are related to the 0.1 K resolution of the temperature sensors, to the existence of thermal leaks in the hydraulic system, and to the numerical uncertainty on the response function explained in section 4.1. In practice, we observe a typical scatter of data points up to 5%, and a similar gap shows up between data sets 1 and 2 of the 1.1 mm canal, taken independently. We choose therefore error bars of $\pm 10\%$ in the h data.

The empirical correlations on h given in the literature are always based on power law on the Reynolds number;

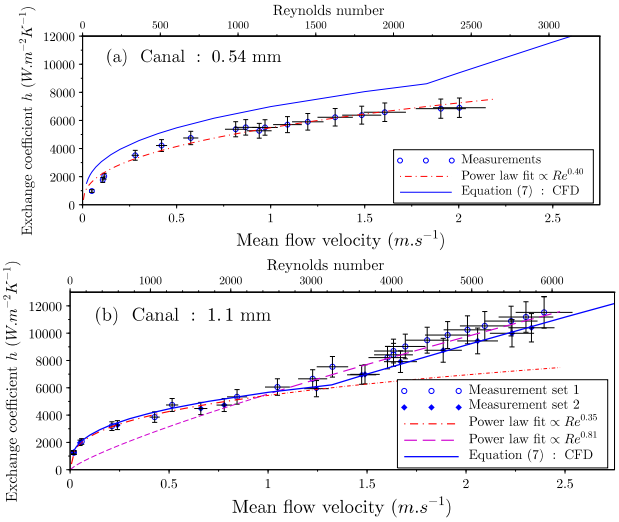

Figure 12: Experimental data for the exchange coefficient, (a) for a 0.54 mm water canal, and (b) for a 1.1 mm water canal. Fits with power law functions are displayed with red dashes. In section 5.3, the experimental data are compared with the combination of the best estimates from Computational Fluid Dynamics, as given by Equation (7), displayed as continuous dark blue line.

the power law exponent is an important element that distinguishes between flow regimes. We present therefore power law fits on the data. In Figure 12(a), the fit, shown in red dash-dots, matches very well the data over the whole measurement range, with Reynolds numbers ranging from 0 to 2400. The power law exponent thus determined is 0.40.

In Figure 12(b), the data present an obvious kink at a flow velocity around 1.1 m/s. We therefore performed a fit for lower velocity values (red dash-dots), yielding a power law exponent of 0.35; and another one for higher velocities (purple long dashes), yielding a power-law exponent of 0.81.

We interpret the kink in Figure 12(b) as the obvious manifestation of the flow regime transition from laminar to weakly turbulent.

5. Comparison with numerical estimates of the exchange coefficient

The experimental data is to be compared with computational results from common numerical methods of Computational Fluid Dynamics (CFD), on the basis of standard models that can be exploited by all laser scientists, without recourse to excessively complex algorithmic tools nor requiring overwhelming computation times. This requires however to bring together thermal tKline:67ransfer within the coolant, Navier-Stokes equations describing fluid motion, and possibly direct absorption within the coolant of pump light, laser light, and amplified spontaneous emission. Full coolant modeling should hence be ideally coupled to modeling of the laser materials, optical windows, and mounts – an ensemble

https://doi.org/10.1017/hpl.2025.10068 Published online by Cambridge University Press

well beyond the scope of the present study[7,13,33].

In the framework of the LEAP-HORIZON project[34], we chose to resort to the COMSOL Multiphysics® version 5.4 software suite, allowing easy coupling to subsequent material analysis and optical calculations. Only the thermal exchange description, which is part of the COMSOL kernel, and the CFD module are used in the following.

We restricted ourselves to model the coolant flows with few well-known approaches: direct numerical solution (DNS) of the Navier-Stokes equations, usually only possible in the laminar regime; the y^+ mixing length model; the Reynolds-Average Navier-Stokes (RANS) $k-\epsilon$ model[12]; the Shear Stress Transport model; and a stationary Large Eddy Simulation (LES) approach. Note that we assume throughout the flow to be stationary.

5.1. Overview of Computational Fluid Dynamic algorithms used

All CFD models for an incompressible fluid start from the mass continuity and from the Navier-Stokes equation, written as

$$\nabla.(\rho\mathbf{u}) = 0 \tag{4}$$

$$\rho(\mathbf{u}.\nabla)\mathbf{u} = -\nabla P + \nabla\mu\Big(\nabla\mathbf{u} + (\nabla\mathbf{u})^T\Big) - \frac{2}{3}\nabla\Big(\mu(\nabla.\mathbf{u})\Big), \tag{5}$$

where $\mathbf{u}$ is the flow velocity field, P the pressure field, μ the dynamic viscosity, ρ the fluid density function. We choose to neglect in Equation (5) any effect of buoyancy – the role of buoyancy in the fluid dynamics of an amplifier head is complex[35], and would deserve further studies, especially for slow flows.

Equation (4) results from mass conservation in an incompressible fluid, while Equation (5) expresses conservation of momentum in a Newtonian fluid with dynamical viscosity μ, yielding a viscosity shear stress tensor K, as the last term of Equation (5).

These fluid equations must be completed by the water heat capacity equation, and by the stationary heat conduction and convection equation

$$\rho C_p\mathbf{u}.\nabla T - \nabla.(\lambda\nabla T) = 0, \tag{6}$$

where λ and C_p are the thermal conductivity and specific heat capacity at constant pressure of water, respectively, and the temperature and velocities should be taken as the average values in the case of a RANS type model like $(k-\epsilon)$.

From this core set of equations, the following standard CFD approaches were investigated:

- These equations are directly solved with the Direct Numerical Simulation approach. This is known to yield accurate solutions in the laminar regime, corresponding in most cases to Reynolds numbers lower than 2300. Laminarity does not mean unidirectional motion however, as the results may indicate a flow regime with recirculation areas, for instance next to the edges of a laser crystal disk, or in any dead end or corner of the water circulation zone. As the Reynolds number increases, the software spends a increased amount of time to converge to a steady state solution; ultimately the calculation no longer converges, which appears as the numerical signature of the onset of weak turbulence. One has to stop the calculation after a fixed number of iterations, which in practice still yields nice-looking results, whose significance is however limited in the turbulent regime.

- The mixing length model, or $y+$ model, is the most simple, and numerically efficient approach. This model assumes that the velocity fluctuations beyond the viscous sub-layer undergo a simple diffusion-like process, over a mixing length l equivalent to a "mean free path". The model assumes that l is null in the viscous sublayer, and increases beyond it linearly as $l = \kappa y$, where $\kappa \simeq 2.5$ is the Von Karman constant and y is the distance to the nearest wall[16]. The Reynolds stresses can then be estimated analytically on the basis of the solution of coupled algebraic laws on a normalized velocity $u^+ = u/u_*$, where u is the flow velocity, and on a normalized spatial dimension $y^+ = y/y_*$. Here u_* is the friction velocity $u_* = \sqrt{(du/dy)\mu/\rho}$, and y_* is essentially the local width of the viscous sublayer. This model predicts a logarithmic behaviour of the flow velocity beyond the viscous sub-layer, up to domain where the velocity saturates to the incoming flow velocity, in the model case of a Blasius flow, namely, a flow with uniform velocity impinging on a single plate parallel to the flow.

- The Reynolds Averaged Navier-Stokes (RANS) approach is intended to predict turbulence levels without capturing their temporal evolution, but estimates the mean turbulence content of the flow. We report calculations with the most standard $k-\epsilon$ approach, but we also tested the closely related $k-\omega$ approach, and the Shear Stress Transport model, often considered to blend the advantages of $k-\epsilon$ and $k-\omega$.

  In the RANS approach, the velocity field $\mathbf{u}$, the pressure field P, the temperature field T are assumed to be the sum of a slowly varying term, and of a fast randomly varying term, whose time-average is zero. Still assuming the fluid to be incompressible, this results in a modified Navier-Stokes equation, that requires the introduction of two new physical quantities: the turbulent kinetic energy k, the turbulence energy decay rate ϵ. The viscosity stress tensor K is then modified to include a turbulent viscosity term, added to the

https://doi.org/10.1017/hpl.2025.10068 Published online by Cambridge University Press

standard kinematic viscosity. The set of equations is closed by two convection equations for k and ϵ, with ad-hoc parameters[12]; a turbulent convection term is also added to the heat conduction-convection in Equation (6).

- Large Eddy Simulations (LES) are usually time-dependent simulations, akin to the Direct Navier-Stokes simulations, thus allowing to describe the spatial and temporal evolution of turbulent vortices, also called eddies. The largest eddies are entirely simulated; however, the energy transfer cascade of large eddies to smaller and smaller eddies is interrupted by a numerical filter, and ad-hoc estimates are used to evaluate the residual Reynolds stresses. We made use of the LES approach with the residual-based variational multiscale with viscosity (RBVMWV) method to evaluate the effect of the smaller vortices. The multi-physics software uses a pseudo-time approach to converge to a stationary solution. While LES calculations are known to require high CPU times, our experience does not show an excessive computing load, but lack of convergence issues, similar to those of the DNS approach.

Following[15], we point out that the use of so-called "wall functions"[19], possibly installed by default in the CFD softwares, should be avoided to compute any heat exchange coefficient. Indeed, in many engineering applications, the flow behaviour immediately next to the wall has little importance, and the wall functions allow one to skip the detailed calculations in the viscous sub-layer, at the expense of the appearance of discontinuities in dynamic and thermodynamic variables at the wall. Figure 15 below will show that use of a wall function results in a velocity field that does not respect the no-slip condition. The resulting predictions for thermal exchange rates do not make sense.

Finally, we remind that CFD methods have a number of intrinsic limitations, as underlined by[12,17]. Most CFD models rely on specific approximations to describe turbulence, whose validity may be difficult to evaluate. The Direct Navier Stokes approach stands out, as it does not involve any model of turbulence; however its successful implementation might be difficult[12]. Secondly, CFD models may be oversimplified with respect to the experimental reality, and neglect such factors as surface roughness, interfacial layers, incident vorticity, etc. Thirdly, the multi-physics tools employing CFD, such as COMSOL, have reached a very high degree of sophistication that actually decreases the scientist's ability to check the subtle numerical interconnections between intertwined physical processes.

5.2. *Numerical implementation*

The CFD approaches described above are applied to a test geometry, depicted in Figure 13, which reproduces the most important features of the experiment, while keeping a moderate computing time.

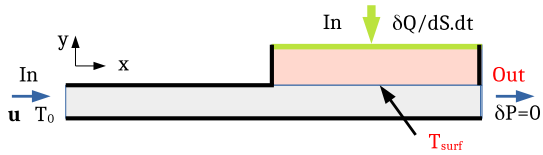

Figure 13: Two-dimensional modeling geometry and set of initial conditions: input velocity (left blue arrow), heat flux (green), initial water temperature (black); output numerical diagnostics: average metal surface temperature, mass-averaged output fluid temperature.

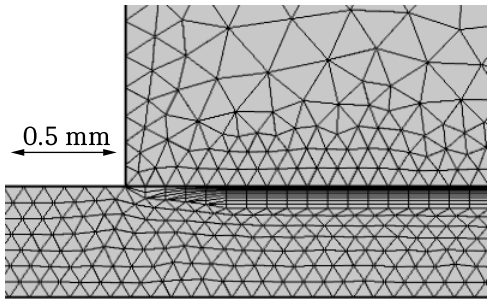

Figure 14: Numerical mesh: zoom onto the entrance region to the thermal interface layer. The metallic heel sits at the top; the lower region is the water canal.

Our 2D model features a water canal, with two parts: a long entrance duct, aimed to let the decay of any vortex induced by the injection conditions, and mimic the experimentally imposed flux calming section; and a part in which the fluid is in contact with a heated metallic heel in its upper part.

The canal width and interface length reproduce the experimental values (0.54 mm or 1.1 mm). The entrance canal length can be taken as identical to the interface length, or longer. In all cases, the flow at the entrance of the exchange region was checked to have reached a stationary average velocity profile.

All boundaries, except the heat injection surface, the exchange interface, and the fluid input and output, are thermally isolated (thick lines). The heat flux dQ/dS is injected uniformly on the upper heel surface S, goes through the metallic layer, of conductivity λ_c and width d_c, then through the thermal layer of the flow. In a 2D geometry, the heat injection surface or exchange surface are given by the common heel and interface length L, taken to correspond to the experimental value ($L = 24$ mm). The heel thickness is taken as 5 mm, smaller than the experimental one – this parameter was checked not to play any significant role. Calling T_S the average temperature at the water-metal interface, and T_0 the initial water temperature, the numerical

https://doi.org/10.1017/hpl.2025.10068 Published online by Cambridge University Press

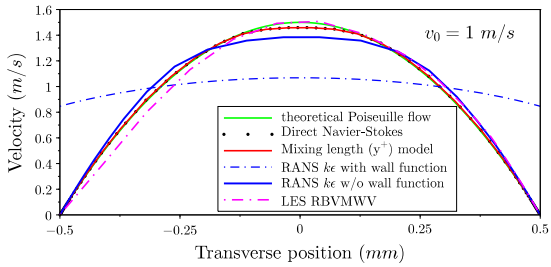

Figure 15: Transverse velocity profiles at *Re*=2000, as computed by the various CFD models examined: theoretical Poiseuille profile, DNS, mixing length model, RANS $k-\epsilon$ with and without wall function, Large Eddy Simulation with the Residual-Based Variational Multiscale With Viscosity method.

exchange coefficient is calculated as $h = P_{th}/S(T_S - T_0)$.

Numerical convergence was checked on all parameters, with respect to the height of the heel, to the incident velocity profile of the incoming flow, and to the value of the injected power. Of particular importance was the definition of the numerical mesh in the thermal layer, namely, the first few hundreds of micrometers immediately below the exchange surface. Figure 14 displays the typical mesh used for the converged computations; while the general mesh follows a triangle structure, we resorted to a very fine rectangular mesh in the thermal layer, with cell heights starting at 3 µm and increasing exponentially up to 70 µm, corresponding to the general triangular mesh of the water flow. These figures are both commensurate with the distance $y_{Re=1}$ to the wall that results in a local Reynolds number $v(y)y/\nu$ of 1: $y_{Re=1} \simeq$ 10 µm, which is an estimate of the local Kolmogorov length scale. Similarly, a fine mesh ($\simeq$ 70 µm) over the remaining water flow turned out to be necessary to reach converged exchange coefficients. In contrast, a rough mesh within the heel was sufficient, with the COMSOL meshing algorithm forcing the mesh size close to the interface to match that of the flow. Numerical convergence with respect to mesh parameters was checked independently in each mesh region: triangular mesh general flow region, rectangular mesh thermal layer, triangular mesh metallic heel.

Figure 15 shows the transverse velocity distributions of a fully established Poiseuille flow, from analytical theory (green); Direct Numerical Simulations (black dots); the mixing length y^+ model (red); RANS with (blue, dot-dashed) and without (blue, continuous) wall functions; and LES simulation (magenta, dot-dashed). Even in the laminar regime, the velocity profile appears flattened by all CFD computations, with respect to the theoretical Poiseuille profile. Agreement between y^+ and DNS is excellent; RANS $k-\epsilon$ with wall functions are completely different from all others.

5.3. Comparisons between experimental data, model-dependent numerical estimates, and empirical correlations

The numerical results from DNS (red line), y^+, RANS $k\epsilon$, SST, and LES calculations can now be compared with our experimental data. The latter are reproduced in Figure 16 as black dots, without the errors bars, for a canal of 0.54 mm (cf Figure 16(a)), and 1.1 mm (cf Figure 16(b)).

DNS and y^+ turn out to be exactly superposed. They display the same "square-root" aspect as the experimental data for the 0.54 mm canal, and for the 1.1 mm data up to a velocity around 1.1 m/s. Agreement is excellent with the latter data; the DNS or y^+ curve stands above the 0.54 mm data, with a 15 % relative difference in the *Re*=1000 range, which remains close to the estimated error bars. While no definitive explanation of the deviation between the DNS and the 0.54 mm experimental data points can be found, we suspect however that a thin oxide layer may have developed over the exchange surface in the course of the 0.54 mm canal experiment, leading to a slightly reduced exchange coefficient.

SST and LES RMVMWV calculations happen to yield similar values of h, which are consistent with, and slightly larger, than the DNS or y^+ results. No kink is observed on either of these four models.

In contrast, the RANS $k-\epsilon$ model predictions do not match the data for the 0.54 mm canal; for the 1.1 mm one, they correctly fit the data for velocities higher than 1.2 m/s, or Reynolds numbers larger than 2700. Our RANS $k-\omega$ predictions are almost identical to the RANS $k-\epsilon$ ones; the $k-\omega$ model does not present any specific advantage with respect to the $k-\epsilon$ one, to describe laser face-cooling.

Interestingly in (b), the y^+ and RANS $k-\epsilon$ models intersect at the position of the kink in the experimental data. For the 0.54 mm canal, the intersection between y^+ and RANS results occurs at a Reynolds number around 2200, close to the highest Reynolds values of the experimental data.

From this comparison, we conclude that the 0.54 mm canal data were taken entirely in a laminar regime; the flow conditions for the 1.1 mm canal are first laminar, then switch to weakly turbulent, and from that point on, are correctly described by the RANS $k-\epsilon$ model.

This can be understood as follows. In the laminar regime, the exact DNS method fully converges, and is the most relevant to describe the heat exchange; once the weakly turbulent regime sets in, DNS fails to converge rigorously and is no longer able to describe adequately the effect of vortices in the flow. In contrast, RANS models like $k-\epsilon$ and $k-\omega$ compute the time-averaged effect of eddies, and the associated turbulent transport, even when there are actually no eddies around in the laminar regime. The prediction of RANS $k-\epsilon$ is therefore meaningless in the laminar regime, but becomes meaningful in the weakly turbulent regime,

https://doi.org/10.1017/hpl.2025.10068 Published online by Cambridge University Press

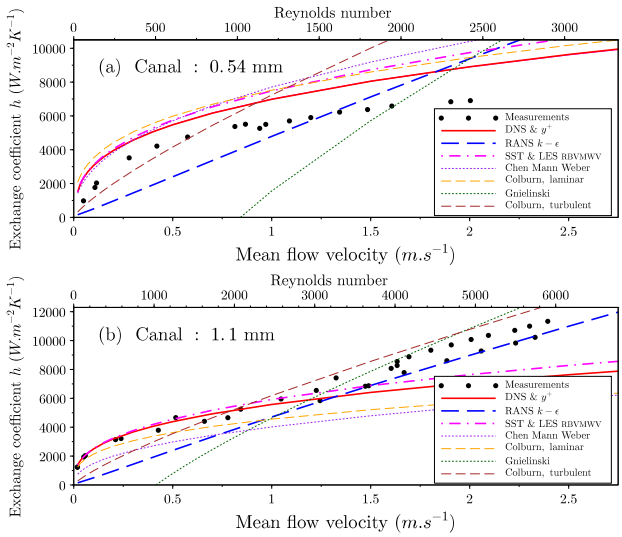

Figure 16: Comparisons between experimental data (same data as in Fig. 12) for the exchange coefficient, (a) for a 0.54 mm water canal, and (b) for a 1.1 mm water canal, and numerical models or empirical laws.

leading to a sudden change in the functional dependence of the exchange coefficient with respect to the Reynolds number. Such a sudden switch was reported by Gnielinski[11] at the laminar to turbulent transition at *Re*=2300.

This reasoning, and the known change of behaviour at the laminar to turbulent transition, lead us to suggest a simple means to compute the exchange coefficient by 2-dimensional Computer Fluid Dynamics:

$$h = \sup(h_{y^+}, h_{\text{RANS } k-\epsilon}), \tag{7}$$

where we use the y^+ approach in the laminar range instead of DNS, since y^+ has no convergence issues and yields the same results for h as DNS.

Figure 12 allows to compare Equation (7) with the experimental data and the fits. For the shallowest canal, the CFD prediction is slightly higher than the data, by about 20%; the kink does not appear experimentally, but the expected transition is within the velocity error bars of the last data point. For the 1.1 mm canal, these combined CFD predictions fit remarkably the data.

This simple equation, which remains to be evaluated in other flow conditions, might be in practice the most useful take-away message of our heat exchange studies.

The analytical laws or empirical correlations do not match as well the experimental data, but are however interesting, and potentially useful to yield estimates without recourse to CFD numerical tools. We therefore test against our data two analytical laws supposed to fit the heat exchange in the laminar regime, and two in the turbulent regime.

In his textbook[36], Koechner advises to consider the correlation supplied by Mann and Weber in 1988[37], who used the formula proposed by Chen and coworkers in 1946[38]. The equation was derived from experimental data for heat transfer in annuli; going to the limit where the annulus radii of curvature reach infinity yields the relation

$$h_{\text{Chen}} = C_L \frac{k}{d_h}\left(\frac{d}{L}\right)^{0.4} Pr^{0.33} Re^{0.45} Gr^{0.05}, \tag{8}$$

where L is the length of the heat exchange section; *Gr* is the Grashof number, characteristic of buoyancy effects and free convection; and C_L is a numeric factor. While Mann and Weber advise to take $C_L = 0.5 \pm 0.1$, we used in Figure 16 a value $C_L = 1.02$, as in the original publication by Chen *et al*. The dependence on the Grashof number, although weak, creates two issues, conceptual and practical: i) why does this correlation include a term of natural convection, while the experiments are made in a forced convection regime; and ii) the Grashof number depends on the temperature difference between wall and liquid, which is an *a priori* unknown value: given a heat deposition rate in a laser amplifier, the temperature difference results from the heat exchange coefficient, which is the value we wish to evaluate. To bypass this loop, our estimate in Figure 16 makes use of the temperature difference obtained numerically by the y^+ approach, with an heat load matching that of our experiment. This somehow cumbersome procedure actually supplies qualitatively reasonable estimates (purple thin dotted line), above the experimental data for the 0.54 mm canal, and below them for the 1.1 mm canal.

We also compare with the Colburn correlation in laminar regime, as advised by the textbook of Battaglia, Kosiak and Puiggali[22]:

$$h^{\text{lam}}_{\text{Colburn}} = 1.86 \frac{k}{d_h}\left(\frac{Re \cdot Pr \cdot d_h}{L}\right)^{0.33}\left(\frac{\mu}{\mu_s}\right)^{0.14}, \tag{9}$$

where μ is the fluid dynamical viscosity at its average temperature in the canal, and μ_s the fluid dynamic viscosity at the wall temperature. Following Mann and Weber, we simply assume $\mu = \mu_s$, which amounts to a small temperature difference approximation. The resulting numerical estimate of the laminar Colburn is represented in orange thin dashes; it overestimates the heat exchange for the 0.54 mm canal, underestimates it for the 1.1 mm canal, like the Chen correlation (cf Equation (8)), but to a significantly lesser extent. The functional dependence on the velocity, ie. the power-law behavior, is also better than that observed with the Chen correlation.

In the weakly turbulent regime, we propose comparisons with the empirical correlation by Gnielinsky[39], as was suggested by Yang[13], and with the Colburn turbulent correlation[22] :

$$h^{\text{turb}}_{\text{Colburn}} = 0.023 \frac{k}{d_h} Re^{0.8}\, Pr^{0.33}. \tag{10}$$

https://doi.org/10.1017/hpl.2025.10068 Published online by Cambridge University Press

The power law in the Reynolds number is quite close to that obtained in our power-law fit of the data. This function is represented in thin brown dashes; for the 0.54 mm canal, it does not fit the data, which makes sense since the flow regime was laminar, and the function is supposed to be valid in a weak turbulence regime. For the 1.1 mm canal, it does run parallel to those experimental data points after the kink in the curve. It overestimates slightly the h coefficient; however, its main drawback is that the intersection with the Colburn laminar correlation does not seem to match the position of the kink observed experimentally.

The Gnielinski correlation reads [39]

$$h_{\mathrm{Gni}} = \frac{k_f \cdot F}{d_h}(Re - 1000)\frac{Pr}{1 + 12.7\sqrt{F}(Pr^{2/3} - 1)}, \quad (11)$$

where $F = (1.82 \cdot \log_{10} Re - 1.64)^{-2}/8$. This function is represented in thin dark green dashes. In contrast to the Colburn turbulent correlation, this estimate does not start at the origin, but at $Re = 1000$. The intersection with the laminar curve for the 1.1 mm canal occurs around $Re = 3000$, consistent with the experimental kink position.

The overall agreement between these correlations and the experimental data is less satisfactory than between CFD calculations and data. From this set of comparisons, we can suggest that the following relation, mimicking Equation (7), might still be of practical interest to design face cooling systems without recourse to CFD tools :

$$h = \sup(h^{\mathrm{lam}}_{\mathrm{Colburn}}, h_{\mathrm{Gni}}). \quad (12)$$

6. Conclusions

From these studies, amplifier maquettes were quite useful to gain insight into the physics of face-cooling of laser multi-slab amplifiers:

- From benchmarking the results of CFD computations and analytical or empirical correlations with the experimental data for heat exchanges, we conclude that the mixing length y^+ model is effective to predict exchange rates in the laminar regime; that the RANS $k - \epsilon$ model is effective to predict exchange rates in the weakly turbulent range. As soon as turbulence sets in, the Nusselt number is dominated by the turbulent eddies. Our proposed formula in Equation (7) should therefore supply good estimates over all regimes. Formulae (9), (11) and (12) can be used together as a fast estimator, but CFD computations turned out to be much more reliable than analytical correlations.

- In the conditions of face-cooling of amplifiers, the pre-transitional range of Reynolds numbers plays a crucial roles. All laboratories testing face-cooling have observed striae. From our axial and side phase images, we point out that these are not an effect of turbulence, but are a pre-transitional hydrodynamic instability, which, in our experimental conditions and following the usual engineering definition of the Reynolds number, starts at $Re = 1000$, whereas the heat exchange measures clear see the onset of turbulence around $Re = 2700$. Figure 9 actually shows that the striae start to decrease at that Reynolds number, indicating that the onset of turbulence may correspond to a break-up of the streaks. Our side-imaging movie may show that, in our specific conditions of water face-cooling, turbulence may be triggered by the detachment from the wall and consequent break-up of the streaks, and not by the usual Tollmien-Schlichting route.

  The striae, or underlying current streaks, appear randomly, with however preferentially zones of prevalence, which vary with the average flow velocity, possibly pointing out a relation with residual velocity-dependent vorticity of the incident flow. The hydrodynamic nature of these pre-transitional streaks remains to be understood.

- Our experiments have revealed the interest of the Reynolds range beyond 10000. In this super-forced thermal regime, the thermally affected zone within the flow remains restricted to a thin layer on the exchange surface, and the striation effect tends to vanish.

To design a water face-cooled laser amplifier, a laser scientist must suppress, or at least strongly mitigate, the striation effect. From our studies, three strategies can be envisioned:

- Bleach optically the striae, by resorting to the index-levelling method proposed by Marion et al. [40];

- a shallow canal approach: remain at Reynolds numbers less than 1000, by decreasing the distance between the slabs, or between slab and window. Reaching values less than 0.5 mm may however be difficult from a mechanical design perspective, which should effectively limit the heat exchange coefficients to ca. 6000 $\mathrm{W.m^{-2}.K^{-1}}$.

- Increase strongly the hydraulic pump pressure, to accelerate dramatically the flow, and reach the super-forced thermal regime. The latter should however be the subject of further studies, which entails several experimental challenges. Hydraulic systems should be developed, able to inject flows with hydraulic pressures of few bars, into millimetric or sub-millimetric single or multiple canals, while keeping precise pressure equilibria to prevent mechanical damage. Other challenges involve the fast time scales required to diagnose the index inhomogeneities, and the reduced index differences.

https://doi.org/10.1017/hpl.2025.10068 Published online by Cambridge University Press

The first strategy can actually be combined with either of the other two; therefore we are confident that these conclusions can pave the way to new generations of high energy laser amplifiers, with average powers in the multi-kW range or higher. Many further studies would still be highly beneficial, on the physics of the striation instability, on the super-forced thermal regime, and on the extremely complex effects of buoyancy in laser face-cooling systems.

Competing interests

The authors declare none.

Acknowledgments

This work is part of the Leap project, supported by Région Nouvelle-Aquitaine (contracts 16005645 and 8384920), and by the European Structural and Investment Funds (contracts 2779610 and 7609710).
It was also supported by CNRS Innovation under the Turbocool project (2022-2023).
Funding and human resources dedicated to the Leap project, as well as administration by Université de Bordeaux, CEA, CNRS, and CELIA administrative unit are gratefully acknowledged. The authors also wish to acknowledge the mechanical expertise of Laurent Merzeau and Franck Blais and to thank them for the precise fabrication of the various maquettes used in this work; and the contribution to experiments and simulations of J. Brandam, A. Mêlé, M. Taleb-Ali, and J. Patfoort.

References

1. A. Zylstra, O. Hurricane, D. Callahan, A. Kritcher, J. Ralph, H. Robey, J. Ross, C. Young, K. Baker, D. Casey, et al. Nature **601**, 542–548 (2022). doi:10.1038/s41586-021-04281-w.
2. T. Tajima and V. Malka. Plasma Phys. Control. Fusion **62**, 034004 (2020). doi:10.1088/1361-6587/ab6da4.
3. S. Banerjee, K. Ertel, P. D. Mason, P. J. Phillips, M. De Vido, J. M. Smith, T. J. Butcher, C. Hernandez-Gomez, R. J. S. Greenhalgh, and J. L. Collier. Opt. Express **23**, 19542–19551 (2015). doi:10.1364/OE.23.019542.
4. D. Albach, M. Loeser, M. Siebold, and U. Schramm. High Power Laser Science and Engineering **7**, e1 (2019). doi:10.1017/hpl.2018.59.
5. J. D. Zuegel, M.J. Shoup, J.H. Kelly, and C. Frederickson. Novel actively cooled split-disk Nd:glass laser amplifier for high-energy applications with improved repetition rate. In *Advanced Solid-State Photonics*, page ATuB1. Optical Society of America, 2011.
6. M. Siebold, M. Loeser, G. Harzendorf, H. Nehring, I. Tsybin, F. Roeser, D. Albach, and U. Schramm. Optics Letters **39**, 3611–3614 (2014). doi:10.1364/OL.39.003611.
7. J. Yi, B. Tu, X. An, X. Ruan, J. Wu, H. Su, J. Shang, Y. Yu, Y. Liao, H. Cao, L. Cui, Q. Gao, and K. Zhang. Opt. Express **26**, 13915–13926 (2018). doi:10.1364/OE.26.013915.
8. R. Chonion, J. M. Sajer, E. Bordenave, F. Le Palud, P.-M. Dalbies, and J. Néauport. Opt. Express **28**, 20162–20176 (2020). doi:10.1364/OE.394271.
9. P. Li, X. Fu, Q. Liu, and M. Gong. J. Opt. Soc. Am. B **30**, 2161 (2013). doi:10.1364/JOSAB.30.002161.
10. X. Ruan, H. Su, B. Tu, J. Shang, J. Wu, J. Yi, H. Cao, Y. Ma, G. Wang, D. Shen, Q. Goa, K. Zhang, and C. Tang. Optics Communications **436**, 26–33 (2019). doi:10.1016/j.optcom.2018.11.069.
11. Volker Gnielinski. Forschung im Ingenieurwesen–Engineering Research 8d. **61**, 240 (1995).
12. H. K. Versteeg and W. Malalasekera. *An introduction to Computational Fluid Dynamics-The Finite Volume Method*. Pearson Education, 2007.
13. H. Yang. Opt. Las. Tech. **150**, 107945 (2022). doi:10.1016/j.optlastec.2022.107945.
14. K. Wang, B. Tu, C. Jia, J. Shang, X. An, Y. Liao, Z. Xu, J. Guo, J. Yi, and Y. Yu. Opt. Express **24**, 15012–15020 (2016). doi:10.1364/OE.24.015012.
15. Roland Sándor Nagymihály, Huabao Cao, Dániel Papp, G Hajas, Mikhail Kalashnikov, Károly Osvay, and Vladimir Chvykov. Optics express **25**, 6664–6677 (2017).
16. Étienne Guyon, Jean-Pierre Hulin, Luc Petit, and Catalin D. Mitescu. *Physical hydrodynamics*. Oxford University Press, 2015. doi:10.1093/oso/9780198517467.001.0001.
17. Jiyuan Tu, Guan-Heng Yeoh, and Chaoqun Liu. *Computational Fluid Dynamics*. Butterworth-Heinemann, 3rd edition, 2018.
18. A.V. Boiko, G.R. Grek, A. V. Dovgal, and V.V. Kozlov. *The Origin of Turbulence in Near-Wall Flows*. Springer, 2002. doi:10.1007/978-3-662-04765-1.
19. Hermann Schlichting and Klaus Gersten. *Boundary-layer theory*. Springer Verlag, 2017. 9th edition.
20. Theodore L. Bergman, Adrienne S. Lavine, Frank P. Incropera, and David P. Dewitt. *Introduction to heat transfer*. Wiley & sons, 2011. 6th edition.
21. L. Graetz. Annalen in der Physik und Chemie **7**, 337 (1885).
22. J.-L. Battaglia, A. Kosika, and J.-R. Puiggali. *Introduction aux transferts thermiques*. Dunod, 2010.
23. P.-M. Dalbies, S. Cavaro, S. Bouillet, Ch. Leymarie, S. Martin, M. Cormier, L. Eupherte, E. Bordenave, N. Blanchot, J. Daurios, and J. Neauport. Optics and Laser Technology **166**, 109448 (2023). doi:10.1016/j.optlastec.2023.109448.
24. J. L. Henares, P. Puyuelo-Valdes, F. Hannachi,

T. Ceccotti, M. Ehret, F. Gobet, L. Lancia, J.-R. Marquès, J. J. Santos, M. Versteegen, and M. Tarisien. Review of Scientific Instruments **90**, 063302 (2019). doi:10.1063/1.5093613.

25. George Bruhat and Alfred Kastler. *Optique*. Masson, 1992. 6th edition completed by P. Bouchareine.
26. Ch. Féral, J. Lhermite, D. Marion, J. Brandam, and Ph. Balcou. Zenodo , (2025). doi:10.5281/zenodo.15593920.
27. J. Mizushima. J. Phys. Soc. Jpn. **89**, 114002 (2020). doi:10.7566/JPSJ.89.114002.
28. M. Barahona, A.F. Rius-Vidales, F. Tocci, P. Ziegler, S. Hein, and M. Kotsonis. Tollmien-Schlichting waves over forward-facing steps : an experimental and numerical study. In *12th International Symposium on Turbulence and Shear Flow Phenomena (TSFP12)*, pages 1–6, 2022.
29. S. J. Kline, W. C. Reynolds, F. A. Schraubt, and P. W. Runstadler. J . Fluid Mech. **30**, 741-773 (1967). doi:10.1017/S0022112067001740.
30. C. B. Lee and J. Z. Wu. Applied Mechanics Reviews **61**, 030802 (2008). doi:10.1115/1.2909605.
31. P. Čolak-Antić and H. Görtler. Wärme- und Stoffübertragung **4**, 25-31 (1971). doi:10.1007/BF01002759.
32. A. V. Boiko and H. H. Chun. Physics of Fluids **16**, 3153–3160 (2004). doi:10.1063/1.1764826.
33. Z. Lin, G. Zhu, W. Zhao, Y. Qiao, M. Wang, H. Wang, and X. Zhu. J. Opt. Soc. Am. B **34**, 1669–1676 (2017). doi:10.1364/JOSAB.34.001669.
34. J. Lhermite, Ch. Féral, D. Marion, A. Rohm, Ph. Balcou, D. Descamps, S. Petit, M.-Ch. Nadeau, and E. Mével. HORIZON laser: a new generation of kw-class ps amplifier. In *International Conference on Advanced Laser Technologies (ALT)*, number 21, page 133. Prokhorov General Physics Institute of Russian Academics of Sciences, 2021.
35. Y.-C. Chen and J. N. Chung. Journal of Fluid Mechanics **325**, 29–51 (1996). doi:10.1017/S0022112096008026.
36. Walter Koechner. *Solid State Laser Engineering*. Springer, 6th edition, 2006. doi:10.1007/0-387-29338-8.
37. K. Mann and H. Weber. J. App. Phys. **64**, 1015-1021 (1988). doi:10.1063/1.341910.
38. C. Y. Chen, G. A. Hawkins, and H. L. Solberg. ASME. Trans. ASME **68**, 99–106 (1946). doi:10.1115/1.4018414.
39. V. Gnielinski. Forschung im Ingenieurwesen A **41**, 8–16 (1975). doi:10.1007/BF02559682.
40. D. Marion, Ph. Balcou, Ch. Féral, A. Rohm, and J. Lhermite. Opt. Lett. **47**, 2850 (2022). doi:10.1364/OL.455616.